JOURNAL OF GEOPHYSICAL RESEARCH, VOL. 90, NO. A12, PAGES 12,271–12,281, DECEMBER 1, 1985

Transient Tropospheric Electric Fields Resulting from Sudden Changes in Ionospheric Conductivity

M. DEJNAKARINTRA,[1] U. S. INAN, AND D. L. CARPENTER

STAR Laboratory, Stanford University, Stanford, California

The transient electric fields that would be generated by sudden changes in the atmospheric conductivity profile are estimated using a theoretical model. The model assumes the existence of a horizontal electric field with a spatial extent of $\geq$ 20-km at 150-km altitude and involves the solution of the boundary value problem in two dimensions. The geomagnetic field lines below 150-km altitude are assumed to be vertical, but the anisotropy of the medium above $\sim$ 70-km altitude is fully accounted for. The computed electric field strength depends sensitively on the size of the source field as well as the conductivitity profile of the atmosphere. In the steady state, a small-scale ($\sim$ 20-km) source field produces relatively weak dc electric fields in the troposphere, whereas a large scale ($\sim$ 100-km) source produces stronger observed fields. On the other hand, during a transient the peak electric fields produced in the case of a small-scale source field can be considerably larger than those due to large-scale source distributions. The more rapid the increase in the slope of the conductivity profile with altitude, the more efficient should be the downward mapping of both transient and steady state fields. Since the transient electric fields are oscillatory and die out at a rate depending on the local conductivity, the ac electric fields at the ground level are found to last longer than those at higher altitudes.

1. INTRODUCTION

Electric field mapping in the earth's atmosphere has been a research subject for more than 20 years. Many researchers [e.g., *Farley*, 1959; *Spreiter and Briggs*, 1961; *Reid*, 1965; *Mozer*, 1970; *Atkinson et al.*, 1971] have studied electrical coupling between the troposphere, ionosphere, and the magnetosphere. The subject involves both mapping of tropospheric electric fields upward into the ionosphere and magnetosphere [e.g., *Park and Dejnakarintra*, 1973; *Dejnakarintra*, 1974] and mapping of ionospheric and magnetospheric electric fields downward into the troposphere [e.g., *Bostrom et al.*, 1973; *Chiu*, 1974; *Volland*, 1974; *Bostrom and Fahleson*, 1974; *Park*, 1976, 1979]. It also involves both dc electric fields [e.g., *Park and Dejnakarintra*, 1973; *Park*, 1976, 1979] and time-varying electric fields [e.g., *Bostrom and Fahleson*, 1974; *Dejnakarintra and Park*, 1974]. In all of these studies, however, the medium in which the electric fields exist is assumed to be time independent.

In this paper we consider the downward mapping of an ionospheric electric field into the troposphere following a "sudden" change in the atmospheric conductivity profile. We limit our formulation to the case of a static magnetic field that is vertical to the earth's surface, so that our results are most applicable at high latitudes. The "sudden" change is assumed to occur within a fraction of a second and to be sustained for a time of the order of at least several seconds. Such changes in ionospheric conductivity can occur as a result of sudden solar particle events (SPE) or particle precipitation into the lower ionosphere. The ionospheric electric field can be of solar wind or ionospheric dynamo origin. Various scale sizes of the field, ranging from 20 km to 3000 km are considered. At mid to high latitudes, the smaller sizes of $\sim$20 to 100 km might be associated with the dayside cusp [e.g., *Maynard et al.*, 1982], with latitudinally narrow regions of intense fields near the premidnight plasmapause [e.g., *Smiddy et al.*, 1977], or with the E field structure of auroral arcs [e.g., *de la Beaujardiere et al.*, 1981].

Evidence that fast changes in ionospheric conductivity occur and that they occur in mid to high latitude regions, where strong and variously structured electric fields are expected, is implicit in reported observations of X ray microbursts in the region poleward of the plasmapause [*Park*, 1978]. Some such microbursts, often with fine structure lasting several hundred milliseconds, have been found to be correlated on a one to one basis with structured VLF wave bursts that propagated on magnetospheric paths [*Rosenberg et al.*, 1981]. Sudden ionospheric perturbations poleward of the plasmapause, apparently induced by whistlers and VLF noise bursts, have also been detected by means of changes in the phase and amplitude of subionospherically propagating signals from the Siple, Antarctica, VLF transmitter [*Carpenter et al.*, 1985].

Theoretical modeling of wave-induced particle precipitation has provided results consistent with experimental findings, indicating that the resulting fluxes may often reach their peak values within a second [*Inan et al.*, 1982; *Chang and Inan*, 1985]. The goal of our study is to estimate theoretically the dc and ac electric fields that would result from such events. Our results should be helpful in assessing the feasibility of using electric field measurements in the troposphere and on the ground for studying precipitation-induced changes in the atmospheric conductivity profile.

The problem formulated here has its counterpart in the field of magnetic measurements, which have recently been used to identify the magnetic effects at ground level of ionospheric perturbations in which the conductivity of the ionosphere is apparently changed [e.g., *Engebretson et al.*, 1983; *Arnoldy et al.*, 1982]. The two problems are complementary,

[1]Now at Department of Engineering, Chulalongkorn University, Bangkok, Thailand.

Paper number 5A8484.
0148-0227/85/005A-8484$05.00

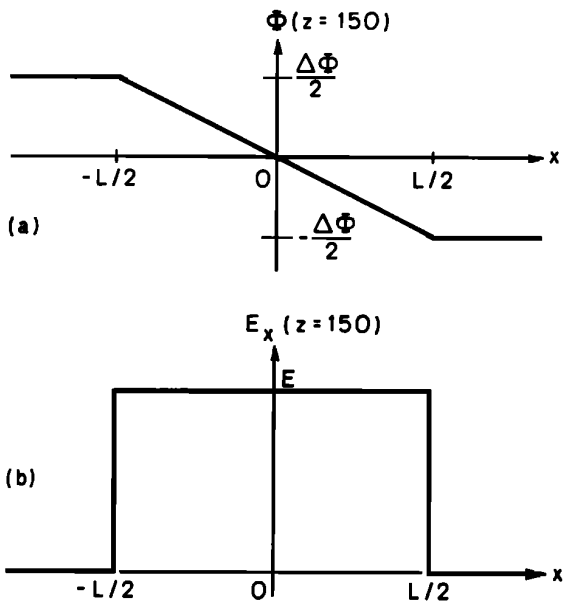

Fig. 1. Assumed source distributions at 150 km altitude. (*a*) Electrostatic potential. (*b*) Horizontal electric field.

involving the rather different physics of magnetic and electric field mapping down through the lower ionospheric layers and atmosphere.

2. THEORY

We first formulate equations for electric fields in the troposphere. To do this, we let the x, y, and z axes be along the north-south, west-east, and vertical directions, respectively, with the origin of the coordinates being on the ground.

At $z = 150$ km altitude, which is at the upper boundary of the region of our interest, we assume the source potential and source electric field to be constant with respect to y but to vary with x as shown in Figure 1. The source is associated with the solar-wind-induced electric field in the magnetosphere. The field distributions shown in Figure 1 are simplified forms of more realistic ones [e.g., *Volland*, 1974; *Heppner*, 1972].

The electrical properties of the atmosphere change significantly between 0 and 150-km altitudes. We therefore divide the space into three regions, which require different treatments, as shown in Figure 2. Below ~70-km altitude the earth's atmosphere consists of gases whose densities are so high that their collision frequencies are large compared to the gyrofrequencies. The effects of the geomagnetic field on the charge carriers in this region are unimportant, and the conductivity of the atmosphere can be considered isotropic. Above ~70-km altitude the gases become less dense, the geomagnetic field has more influence on the charge carriers and the atmospheric conductivity becomes anisotropic. Above ~150-km altitude, the conductivity along the geomagnetic field lines becomes very large compared to the transverse conductivities; thus the magnetic field lines can be considered equipotentials. Since we are predominantly concerned with phenomena occurring poleward of L ~4, the geomagnetic field lines are assumed to be straight and vertical.

Steady State dc Electric Fields in an Anisotropic Layer

From Maxwell's equations for dc electric and magnetic fields, i.e., $\nabla \times \mathbf{E} = 0$ and $\nabla \times \mathbf{H} = \mathbf{J}$, we can write basic equations for the fields in a "source-free," anisotropic layer of the atmosphere as

$$\mathbf{E} = -\nabla\Phi \qquad \nabla \cdot \mathbf{J} = 0 \quad \mathbf{J} = (\vec{\sigma})\mathbf{E} \tag{1}$$

where $\mathbf{E}$ is the electric field intensity, Φ is the electrostatic potential, $\mathbf{J}$ is the conduction current density, and $\vec{\sigma}$ is the conductivity tensor of the medium. Here "source-free" is meant to indicate that there is no current injection inside the region of interest. However, there may be polarization charge due to the anisotropic conductivity of the medium and displacement current due to temporal variation of the electric field.

In the region near the north pole, $\vec{\sigma}$ in the Cartesian coordinate system [e.g., *Rishbeth and Garriott*, 1969], is given by

$$\vec{\sigma} = \begin{pmatrix} \sigma_P & \sigma_H & 0 \\ -\sigma_H & \sigma_P & 0 \\ 0 & 0 & \sigma_0 \end{pmatrix} \tag{2}$$

where σ_0, σ_P, σ_H are the specific conductivity, Pedersen conductivity, and Hall conductivity, respectively. Equation (2) gives the x, y, and z components of $\mathbf{J}$ as

$$J_x = \sigma_P E_x + \sigma_H E_y \qquad J_y = \sigma_P E_y - \sigma_H E_x \qquad J_z = \sigma_0 E_z \tag{3}$$

We assume the medium to be homogeneous, so that σ_0, σ_P, and σ_H are constants independent of x, y, and z. We also consider the fields to be constant with respect to y. Under these assumptions, equations (1)–(3) combine to yield

$$\partial^2\Phi/\partial x^2 + (1/b^2)\partial^2\Phi/\partial z^2 = 0 \tag{4}$$

where

$$b = \sqrt{\sigma_P/\sigma_0} \tag{5}$$

Solving equation (4) for Φ by the method of separation of variables and using the relation in equation (1) with

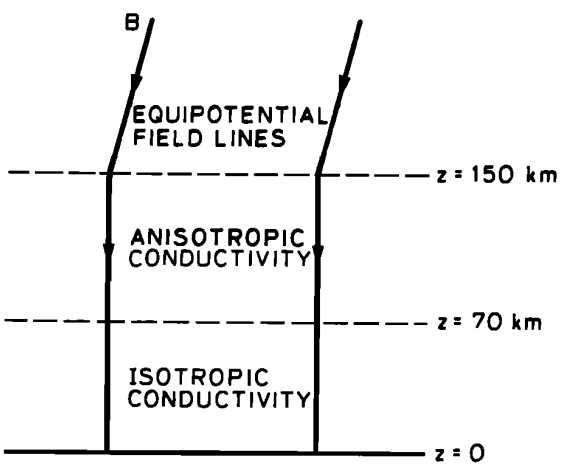

Fig. 2. A simplified sketch of the high-latitude geomagnetic field and three different regions of its influence.

$\partial\Phi/\partial y = 0$, we obtain the dc electric fields in the anisotropic medium [*Dejnakarintra*, 1983], as

$$E_x(x,z) = \{A_1 \sin(k_x x) + B_1 \cos(k_x x)\} \{A_2 e^{-k_x bz} + B_2 e^{k_x bz}\} \quad (6a)$$

$$E_y(x,z) = 0 \quad (6b)$$

$$E_z(x,z) = \{A_1 \cos(k_x x) - B_1 \sin(k_x x)\} \{bA_2 e^{-k_x bz} - bB_2 e^{k_x bz}\} \quad (6c)$$

where A_1, A_2, B_1, and B_2 are arbitrary constants and k_x is the spatial wave number in the x direction.

Steady State dc Electric Fields in an Isotropic Layer

Since an anisotropic medium with the conductivity tensor $\vec{\sigma}$ in equation (2) becomes an isotropic medium with scalar conductivity σ when $\sigma_0 = \sigma_P = \sigma$ and $\sigma_H = 0$, we can obtain electric field expressions for the isotropic medium from equations (6) by simply setting $b = 1$.

We let electric and magnetic fields in the atmosphere be in a steady state at time $t < 0$. At $t = 0$ we allow the conductivity of the medium to change suddenly as a step function of time. To find the initial conditions, we assume the electric and magnetic fields to be continuous with respect to time at $t = 0$, i.e., we let

$$\mathbf{E}(0^+) = \mathbf{E}(0^-) \quad (7)$$

$$\mathbf{H}(0^+) = \mathbf{H}(0^-) \quad (8)$$

This assumption is justified by the capacitive and inductive properties (ϵ_0 and μ_0) of the atmosphere.

Since at $t = 0^-$ the fields are in a steady state, equation (1) yields another condition:

$$\nabla \cdot \mathbf{J}(0^-) = 0 \quad (9)$$

We now consider the electric fields at times $t > 0$.

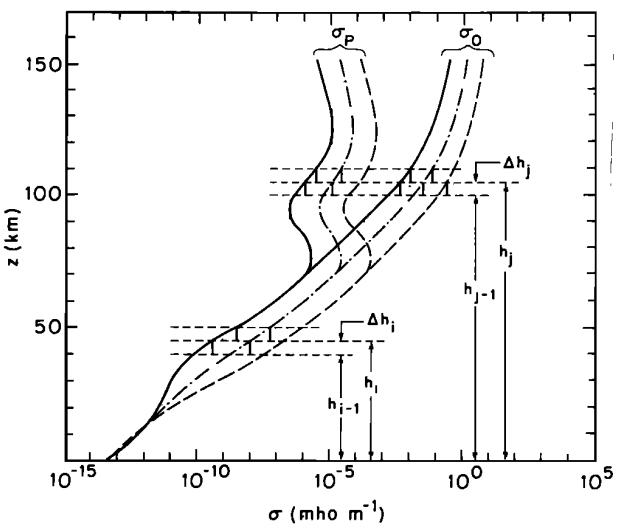

Fig. 3. Slab model of the conductivity profiles of the polar atmosphere under the undisturbed condition (solid curves), typical solar particle events (dot-dash curves), and extreme solar particle events (dashed curves).

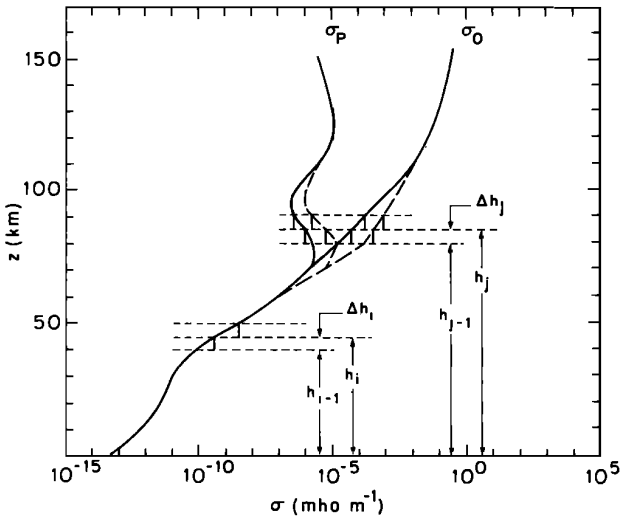

Fig. 4. Slab model of the polar atmosphere under the undisturbed condition (solid curves) and during energetic electron precipitation (dashed curves).

Transient Electric Fields in an Anisotropic Layer

We show in the appendix the equations for time-varying electromagnetic fields in an anisotropic layer of the earth's atmosphere where the conductivity tensor is a function of time. We also discuss therein two equivalent approaches to solve the equations. The first approach begins observation of the fields at $t=0^-$ and includes current density impulses due to a step change in the conductivities at $t=0$, whereas the second one begins at $t=0^+$ and lets the effects of the current density impulses be taken care of by continuity of electric and magnetic fields at $t=0$.

We choose, for simplicity, to follow the second approach and express the field equations as

$$\nabla \times \mathbf{E} = -(\mu_0)\frac{\partial \mathbf{H}}{\partial t} \qquad \nabla \times \mathbf{H} = \mathbf{J} + (\epsilon_0)\frac{\partial \mathbf{E}}{\partial t} \qquad \mathbf{J} = (\vec{\sigma})\vec{E} \quad (10)$$

where, for $t > 0$, the conductivity tensor $\vec{\sigma}$ is constant, independent of time.

Taking Laplace transforms on equations (10) with respect to time t, we obtain

$$\begin{aligned} \nabla \times \mathbf{E}_s &= -\mu_0\{s\mathbf{H}_s - \mathbf{H}(0^+)\} \\ \nabla \times \mathbf{H}_s &= \mathbf{J}_s + \epsilon_0\{s\mathbf{E}_s - \mathbf{E}(0^+)\} \\ \mathbf{J}_s &= (\vec{\sigma})\mathbf{E}_s \end{aligned} \quad (11)$$

where $\mathbf{E}_s, \mathbf{H}_s$, and $\mathbf{J}_s$ are the Laplace transformed functions corresponding to $\mathbf{E}, \mathbf{H}$, and $\mathbf{J}$, respectively.

The components of $\mathbf{J}_s$, similar to those in equations (3), are

$$\begin{aligned} J_{sx} &= \sigma_P E_{sx} + \sigma_H E_{sy} \\ J_{sy} &= \sigma_P E_{sy} - \sigma_H E_{sx} \\ J_{sz} &= \sigma_0 E_{sz} \end{aligned} \quad (12)$$

Manipulation of Eqs. (11) [*Dejnakarintra* 1983] yields

$$\begin{aligned} \nabla^2 \mathbf{E}_s - \mu_0 s\{\mathbf{J}_s + \epsilon_0 s\mathbf{E}_s\} &= -\mu_0\epsilon_0 s\mathbf{E}(0^+) \\ &- \mu_0\mathbf{J}(0^+) - \mu_0\epsilon_0\mathbf{E}'(0^+) + \nabla(\nabla \cdot \mathbf{E}_s) \end{aligned} \quad (13)$$

where

$$\nabla \cdot \mathbf{E}_s = (\sigma_0 + \epsilon_0 s)^{-1} \left\{ (\sigma_0 - \sigma_P) \left(\frac{\partial E_{sx}}{\partial x} + \frac{\partial E_{sy}}{\partial y} \right) - \sigma_H \left(\frac{\partial E_{sy}}{\partial x} - \frac{\partial E_{sx}}{\partial y} \right) \right\} + \epsilon_0 \nabla \cdot \mathbf{E}(0^+) \tag{14}$$

$$\nabla \cdot \mathbf{E}(0^+) = (1 - b_-^2) \left(\frac{\partial E_x(0^+)}{\partial x} + \frac{\partial E_y(0^+)}{\partial y} \right)$$
$$b_- = \sqrt{\frac{\sigma_P^-}{\sigma_0^-}} \tag{15}$$

and σ_0^- and σ_P^- are the values at $t < 0$ of the specific and Pedersen conductivities, respectively.

We consider spatial Fourier components of the fields in the following form:

$$E_u(x, z, t) = e^{ik_x x} e^{ik_z z} e_u(t)$$
$$E_{su}(x, z, s) = e^{ik_x x} e^{ik_z z} e_{su}(s) \tag{16}$$

where $u = x, y$, or z and $E_{su}(x, z, s)$ and $e_{su}(s)$ are the Laplace transformed functions of $E_u(x, z, t)$ and $e_u(t)$, respectively.

Using the expression for $\mathbf{E}_s$ in equation (16) and the relation in equation (13) and decomposing $\mathbf{E}_s$ into three coordinate components, we arrive at

$$\{-(k_x^2 + k_z^2) - \mu_0 s(\sigma_P + \epsilon_0 s) + \left(\frac{\sigma_0 - \sigma_P}{\sigma_O + \epsilon_0 s} \right) k_x^2\} e_{sx}(s) - \{\mu_0 \sigma_H s + \left(\frac{\sigma_H}{\sigma_0 + \epsilon_0 s} \right) k_x^2\} e_{sy}(s) = -\mu_0(\sigma_P + \epsilon_0 s) e_x(0^+) - \mu_0 \epsilon_0 e_x'(0^+) - \{\frac{(1 - b_-^2)\epsilon_0}{\sigma_0 + \epsilon_0 s}\} k_x^2 e_x(0^+) \tag{17a}$$

$$\{-(k_x^2 + k_z^2) - \mu_0 s(\sigma_P + \epsilon_0 s)\} e_{sy}(s) + \mu_0 \sigma_H s e_{sx}(s) = -\mu_0 \epsilon_0 e_y'(0^+) + \mu_0 \sigma_H e_x(0^+) \tag{17b}$$

$$\{-k_x^2 - \mu_0 s(\sigma_0 + \epsilon_0 s)\} e_{sz}(s) = -\mu_0(\sigma_0 + \epsilon_0 s) e_z(0^+) - \mu_0 \epsilon_0 e_z'(0^+) - k_x k_z e_{sx}(s) \tag{17c}$$

Equations (17a)–(17c) result in the following expressions:

$$e_{sx}(s) = \frac{\Delta_x}{\Delta} \qquad e_{sy}(s) = \frac{\Delta_y}{\Delta} \qquad e_{sz}(s) = \frac{\Delta_z}{\Delta} \tag{18}$$

where

$$\Delta = p_5(s) \tag{19}$$

$$\Delta_x = p_4(s) e_x(0^+) + p_3(s) e_x'(0^+) + p_2(s) e_y'(0^+) \tag{20}$$

$$\Delta_y = q_1(s) e_x(0^+) + q_2(s) e_x'(0^+) \tag{21}$$

$$\Delta_z = r_4(s) e_z(0^+) + r_3(s) e_z'(0^+) \tag{22}$$

$$e_x'(0^+) = -\left\{ \frac{(\sigma_P - \sigma_P^-)}{\epsilon_0} \right\} e_x(0^+) \tag{23a}$$

$$e_y'(0^+) = \left\{ \frac{(\sigma_H - \sigma_H^-)}{\epsilon_0} \right\} e_x(0^+) \tag{23b}$$

$$e_z'(0^+) = -\left\{ \frac{(\sigma_0 - \sigma_0^-)}{\epsilon_0} \right\} e_z(0^+) \tag{23c}$$

In equations (19)–(22), $p_i(s), q_i(s)$, and $r_i(s)$ are polynomials of degree i in s whose coefficients are functions of $k_x, k_z, \mu_0, \epsilon_0, \sigma_0, \sigma_P, \sigma_H$, and b_- [*Dejnakarintra*, 1983]. The term σ_H^- in equation (23b) is the Hall conductivity at $t < 0$.

The inverse Laplace transform of equation (18) gives the time function $e_u(t)$, where $u = x, y$, or z, as

$$e_u(t) = \mathcal{L}^{-1}\{e_{su}(s)\} \tag{24}$$

Transient Electric Fields in an Isotropic Layer

We obtain the expressions for transient electric fields in an isotropic layer of the atmosphere by setting $\sigma_0 = \sigma_P = \sigma, \sigma_H = 0, \sigma_0^- = \sigma_P^- = \sigma^-, \sigma_H^- = 0$, and $b_- = 1$ in equations (19)–(23). This leads to

$$e_{su}(s) = \frac{s e_u(0^+) + \{(\sigma/\epsilon_0) e_u(0^+) + e_u'(0^+)\}}{s^2 + (\sigma/\epsilon_0)s + (k_x^2 + k_z^2)/(\mu_0 \epsilon_0)} \quad \{u = x, y, z\} \tag{25}$$

$$e_u(t) = \mathcal{L}^{-1}\{e_{su}(s)\} \tag{26}$$

where

$$e_u'(0^+) = -\{\frac{(\sigma - \sigma^-)}{\epsilon_0}\} e_u(0^+) \tag{27}$$

3. ELECTRIC FIELD CALCULATIONS

In this section, we present a conductivity profile of the atmosphere, boundary conditions to be used, and solution of the boundary value problem of interest.

Model Conductivity Profiles

Figures 3 and 4 show conductivity profiles of the earth's atmosphere under normal and disturbed conditions, as the solid curves and dashed curves, respectively. The solid curves in both figures are obtained from *Reagan et al.* [1980] for the altitude range 0–70 km and from *Park and Dejnakarintra* [1974] and *Park* [1979] for the altitude range 70–150 km. The dashed curves in Figure 3, for conductivity profiles during solar particle events (SPE), and those in Figure 4, for profiles during energetic electron precipitation, are obtained from the data given by *Reagan et al.* [1980] and *Doolittle* [1982], respectively. In these figures we also show vertical stratification of the atmosphere into several horizontal slabs of homogeneous conductivity, to which the electric field expressions derived earlier can be applied. We choose the thickness of each atmospheric slab to be 1 km, based on previous work on a similar problem [*Dejnakarintra*, 1974].

Boundary Conditions

In applying the electric field expressions derived earlier to the various slabs of the atmosphere between 0-km and 150-km altitudes, we will use the following boundary conditions:

1. The horizontal electric fields $E_x = E_y = 0$ at ground level ($z = 0$). This condition corresponds to the assumption of a perfectly conducting ground, which is justified by the fact that the conductivity of the earth is very large compared to that of the air at ground level.

2. At the altitude $z = 150$ km, the horizontal electric field E_x of the 150th atmospheric layer is identical to the source electric field, whose steady state distribution is shown in Figure 1*b* and can be expressed as

$$E_{x,ss}(x, z = 150km) = Ep_{L/2}(x) = \int_0^\infty C(k_x)\cos(k_x x)dk_x \tag{28a}$$

where

$$C(k_x) = \frac{2E}{\pi}\left(\frac{\sin(k_x L/2)}{k_x}\right) \tag{28b}$$

3. E_x and E_y are continuous at all other interface boundaries of the various slabs.

4. The total current density, $J_{z,total}$, which is the sum of the conduction current density $\sigma_0 E_z$ and the displacement current density $\epsilon_0 E_z'$, is continuous at the interface boundaries. Under steady state conditions this simply reduces to continuity of the conduction current density $\sigma_0 E_z$.

Calculation of Steady State dc Electric Fields

For dc electric fields in an atmospheric slab between 0-km and 150-km altitudes, we use the field expressions from equations (6*a*) and (6*c*) and from equation (28*a*) to write

$$E_{x,i}(x,z) = \int_0^\infty C(k_x)\cos(k_x x)\{A_i(k_x)e^{-k_x b_i z_i} + B_i(k_x)e^{k_x b_i z_i}\}dk_x \tag{29a}$$

$$E_{z,i}(x,z) = -\int_0^\infty C(k_x)\sin(k_x x)\left\{b_i A_i(k_x)e^{-k_x b_i z_i} - b_i B_i(k_x)e^{k_x b_i z_i}\right\}dk_x \tag{29b}$$

where $z_i = z - h_{i-1}$ is the vertical distance in the ith atmospheric slab, z is the true altitude of the observation point, h_{i-1} is the base altitude of the ith slab, b_i=1 for an isotropic slab and $b_i = \sqrt{\sigma_{P,i}/\sigma_{0,i}}$ for an anisotropic slab, with $\sigma_{P,i}$ being the Pedersen conductivity of the ith slab and $\sigma_{0,i}$ being the specific conductivity of the ith slab, $i = 1, 2, 3, ..., 150$.

$A_i(k_x)$ and $B_i(k_x)$ in equations (29*a*) and (29*b*) are constants with respect to slab number i but depend on the spatial wave number k_x. They can be evaluated by matching the boundary conditions at the top and bottom surfaces of the ith slab. (Details of the procedure are given by *Dejnakarintra* [1983]). Numerical values of the dc electric fields $E_x(x,z)$ and $E_z(x,z)$ obtained from the integrals in equations (29*a*) and (29*b*) will be given later.

Calculation of Transient Electric Fields

From equations (29*a*) and (29*b*) we know that the steady state field component with spatial wave number k_x varies as $\exp(\pm k_x b_i z_i)$, where z_i is the vertical distance within the ith slab. Since we have the dc electric fields as initial conditions of the transient electric fields, then we must express the transient fields with wave number k_x as functions that synthesize $\exp(\pm k_x b_i z_i)$ at $t = 0$. To do this, we Fourier analyze $\exp(\pm k_x b_i z_i)$ with respect to z_i, let the resulting Fourier components in the new dimension have different wave numbers k_z, and use these two-dimensional components as the initial fields $e_u(0^+)$ in equations (17), (23), (25), and (27). At any time t we can find the z_i variation of the transient field component with wave number k_x by summing over the two-dimensional field components of different wave numbers k_z. Finally, we calculate the overall field $E_u(x,z,t)$ by integrating field components of different wave numbers k_x.

Expressed mathematically, the overall transient electric fields are

$$E_{v,i}(x,z,t) = \int_0^\infty C(k_x)\cos(k_x x)B_i(k_x)\left\{e_{v,i,1}(k_x,z_i,t) + R_i(k_x)e_{v,i,2}(k_x,z_i,t)\right\}dk_x \tag{30a}$$

$$E_{z,i}(x,z,t) = -\int_0^\infty C(k_x)\sin(k_x x)B_i(k_x)\left\{e_{z,i,1}(k_x,z_i,t) + R_i(k_x)e_{z,i,2}(k_x,z_i,t)\right\}dk_x \tag{30b}$$

where $v = x$ or y. Here, $B_i(k_x)$ and $R_i(k_x)$ are constants with respect to i but depend on k_x and can be evaluated from matching the boundary conditions at the top and bottom surfaces of the ith slab at the time instant t of interest [*Dejnakarintra*, 1983].

The functions $e_{u,i,j}(k_x,z_i,t)$ in equations (30*a*) and (30*b*), where $u = x, y$, or z and $j = 1$ or 2, can be expressed as Fourier series as follows:

$$e_{v,i,j}(k_x,z_i,t) = \xi_{v0,i,j}(k_x,k_z=0,t) + \sum_{n=1}^{\infty}\xi_{vn,i,j}(k_x,k_z=nk_{z0},t)\cos(nk_{z0}z_i) \tag{31a}$$

for $v = x, y$ and

$$e_{z,i,j}(k_x,z_i,t) = (C_{i,j} + K_{i,j}z_i)\xi_{z0,i,j}(k_x,k_z=0,t) + \sum_{n=1}^{\infty}\xi_{zn,i,j}(k_x,k_z=nk_{z0},t)\sin(nk_{z0}z_i) \tag{31b}$$

where

$$k_{z0} = \frac{\pi}{\Delta h} \tag{31c}$$

The quantity Δh in equation (31*c*) is the thickness (= 1 km) of each atmospheric slab. The functions $\xi_{un,i,j}$ appearing in equations (31*a*) and (31*b*) are the functions $e_u(t)$ in equations (24) and (26) for an anisotropic slab and an isotropic slab, respectively. The function $(C_{i,j} + K_{i,j}z_i)$ in equation (31*b*) is obtained from applying linear interpolation to the function $\exp(\pm k_x b_i z_i)$ in the range $0 \le z_i \le \Delta h$ [*Dejnakarintra*, 1983].

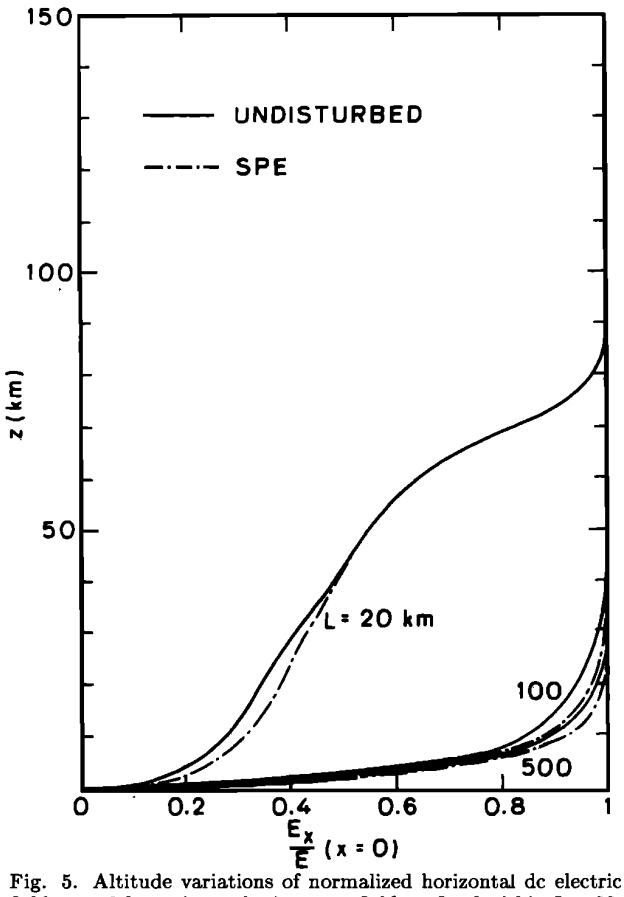

Fig. 5. Altitude variations of normalized horizontal dc electric field at x=0 for an ionospheric source field confined within L = 20, 100, and 500 km.

At $t = 0$, the Fourier series in equations (31a) and (31b) must satisfy the initial steady state conditions, i.e.,

$$e_{x,i,j}(k_x, z_i, 0) = \exp(\pm k_x b_{-,i} z_i) \qquad e_{y,i,j}(k_x, z_i, 0) = 0 \tag{32a}$$

$$e_{z,i,j}(k_x, z_i, 0) = \pm(-b_{-,i}) \exp(\pm k_x b_{-,i} z_i) \tag{32b}$$

where the values 1 and 2 of j correspond to the + and − signs in the ± symbol. In equations (32a) and (32b) we have used $b_{-,i}$ instead of b_i to indicate the initial steady state at $t < 0$. Precisely,

$$b_{-,i} = \left\{ \begin{array}{ll} \dfrac{1}{\sqrt{\sigma^-_{P,i}/\sigma^-_{0,i}}} & \begin{array}{l}\text{for an isotropic slab} \\ \text{for an anisotropic slab}\end{array} \end{array} \right\} \tag{32c}$$

where $\sigma^-_{0,i}$ and $\sigma^-_{p,i}$ are the specific and Pedersen conductivities in the ith atmospheric slab at $t < 0$.

At $t = 0$, the values of $\xi_{un,i,j}$ determined from the Fourier series representations of equations (32a) and (32b) are used as the initial conditions $e_u(0^+)$ for determining $e_u(t)$ from equations (24) and (26).

At any time t, the functions $e_{x,i,j}$ and $e_{z,i,j}$ in equations (31a) and (31b) depend on k_x and z_i only. We can evaluate $B_i(k_x)$ and $R_i(k_x)$ in equations (30a) and (30b) by matching the boundary conditions as was done in the case of dc electric fields. Having done this, we proceed to evaluate the integrals in equations (30a) and (30b) for the overall fields $E_{u,i}(x, z, t)$.

4. RESULTS

We now present numerical results from calculations of electric fields under both steady state and transient conditions.

Distribution of dc Electric Field E_x

For steady state dc electric fields we assume the source field E_x to have an x distribution as given in Figure 1b and calculate the resulting electric fields E_x and E_z in the troposphere. Figure 5 shows the z distribution of E_x/E at $x = 0$ for the source scale length L of 20, 100, and 500 km and the conductivity profiles in Figure 3. The solid curves in Figure 5 correspond to the undisturbed conductivity profile (solid curves) in Figure 3 and the dot-dash curves correspond to the disturbed conductivity profile (dot-dash curves) in Figure 3. We can see from Figure 5 that the increase in conductivity of the atmosphere produces a slight increase in dc electric field E_x at altitudes below ~40 km only. At an altitude of ~30 km, where the electric fields are usually measured by balloon-borne instruments, E_x at L = 20 km increases by ~4%, that at L = 100 km increases by ~ 1%, and that at $L \geq 500$ km does not increase significantly. The reason for this is that a shorter scale-length field is more

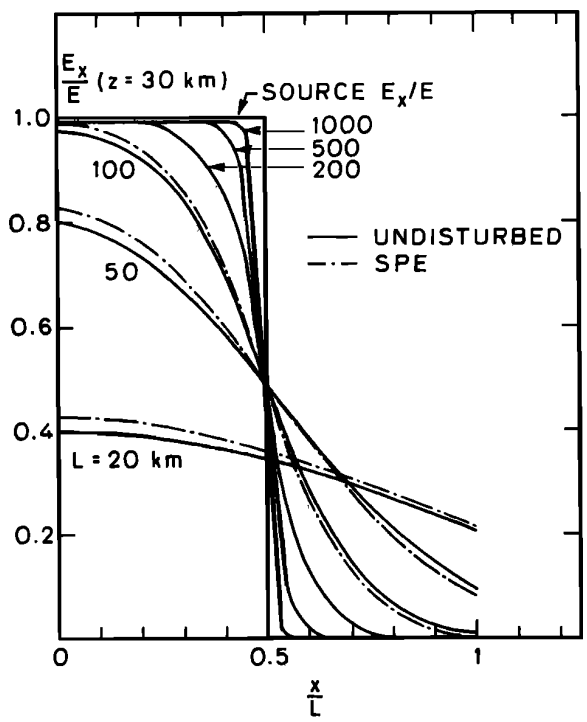

Fig. 6. Normalized horizontal dc electric field at z=30 km plotted against normalized horizontal distance. The straight line labeled "source E_x/E" represents the normalized source electric field at z=150 km.

sensitive to a change in the conductivity profile than is a larger scale-length field.

For a change in the conductivity profile due to electron precipitation as shown by the dashed curves in Figure 4, we obtain results similar to those in Figure 5 but with a much smaller percentage increase in E_x. The smaller change in E_x in this latter case is due to the fact that the new conductivity profile (dashed curves) consists of a part with increasing slope and another part with decreasing slope; their effects tend to cancel one another.

Figure 6 shows the curves of E_x/E versus x/L at $z =$ 30 km for some values of scale-length L. The solid curves correspond to the undisturbed conductivity profile, and the dot-dash curves correspond to the disturbed one (dot-dash curves) of Figure 3. For the purpose of illustration, only three dot-dash curves are shown, for E_x at $L = 20$, 50, and 100 km. The straight line labeled "source E_x/E" is the distribution of the normalized horizontal source field at 150-km altitude.

Comparison among the solid curves in Figure 6 indicates that E_x suffers increasing attenuation as L decreases and becomes more smeared out in the x direction. Only fields at a source scale-length $L \geq 500$ km have their x distribution curves close to that of the source field, though the corners of the curves are rounded. The smearing and rounding in the distribution curves for E_x are due to loss in component fields with higher spatial wave number k_x as they map down from 150-km altitude to 30-km altitude. Under the disturbed condition the dc field E_x shown by the dot-dash curves in Figure 6 changes by a few percent from the undisturbed condition, and its x distribution is similar to that under the undisturbed condition.

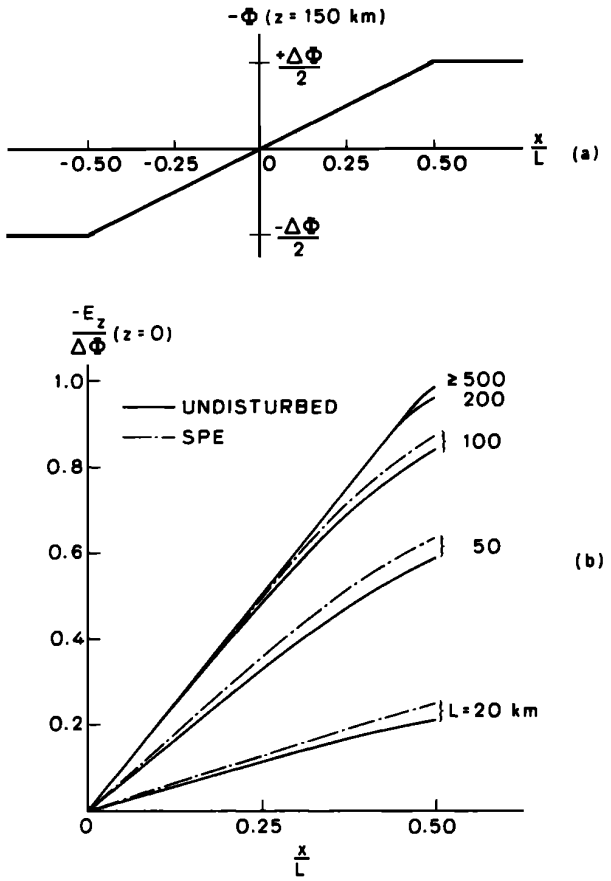

Fig. 7. The inverted distributions of (a) the assumed source potential and (b) the corresponding vertical dc electric field on the ground for several values of the source scale-length L. The vertical electric field is normalized to the assumed source potential difference.

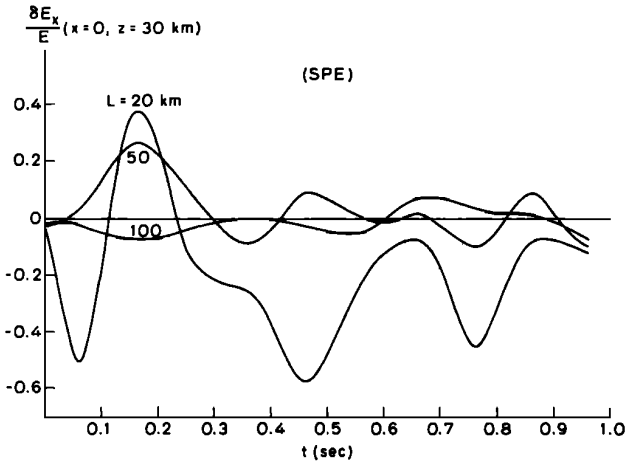

Fig. 8. Smoothed variations of the net normalized horizontal transient electric field following a sudden change in the conductivity profile from the solid curves to the dot-dash curves in Figure 3.

Distribution of dc Electric Field E_z

We show in Figure 7a the inverted potential distribution at $z = 150$ km that corresponds to the horizontal source electric field in Figure 5. And in Figure 7b we show the x distribution of $-E_z$ at $z = 0$, normalized to the potential drop $\Delta\Phi$ of Figure 7a. For a source scale-length $L >\sim 200$ km, the imposed Φ variation is accurately reproduced by the E_z curves. For smaller values of L, the curves become smeared out as in the x distribution of E_x described in the previous subsection. Under the disturbed condition, where there is an increase in conductivity of the atmosphere above 15-km altitude, the dot-dash curves in Figure 7b show an increase of a few percent in the magnitude of E_z at $z = 0$ from that under the undisturbed condition.

The z variation of the dc electric field E_z can be obtained from the conductivity profiles of Figures 3 and 4, since E_z varies approximately as $1/\sigma_0$. The results from dc electric field calculations as shown in Figures 5–7 agree with those obtained previously using a numerical method [*Park*, 1976].

Time Variation of Net Transient Electric Field δE_x

In calculating transient electric fields, we define the source field E_x at $z = 150$ km and $t = 0$ to have the x distribution as in Figure 1. As time t increases, we let this source field decay toward zero in such a way that its strength and x distribution depend on properties of the atmosphere above 150-km altitude. This condition corresponds to sudden turning off of the original source field in the magnetosphere at time $t = 0$. For a sudden increase in the conductivity of the earth's atmosphere at $t = 0$, we calculate two sets of transient electric fields, one set using conductivity elements both

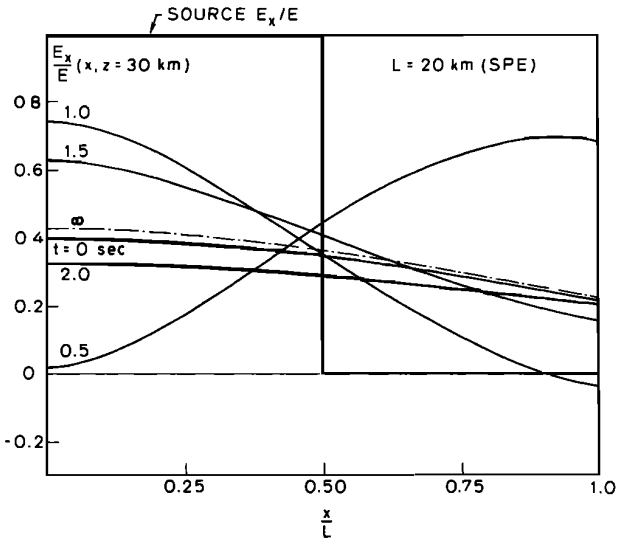

Fig. 9. Normalized horizontal transient electric field at z=30 km plotted against normalized horizontal distance at several time instants. The straight line labeled "source E_x/E" represents the normalized source electric field at 150-km altitude.

before and after the increase and the other set using only the conductivity elements after the increase. The difference of the transient electric fields calculated from these two different conditions is a net transient field that will be added to the steady state dc electric field under the new conductivity profile in order to constitute the total transient electric field. (The reason for this manipulation is given by *Dejnakarintra* [1983].) The results from transient electric field calculations are as follows.

Figure 8 shows a smoothed time variation of normalized net transient electric field $\delta E_x/E$ at $x = 0$ and $z = 30$ km after the conductivity profile suddenly changes from the solid curves of Figure 3 to the dot-dash curves of Figure 3. The original data points used to plot time variation of $\delta E_x/E$ before it is smoothed are obtained discretely for every 0.02 s in the time interval $0 \leq t \leq 1$ s and for every 0.05 s in the interval $1 \leq t \leq 2$ s. The smoothing is done by averaging the fields within 20 subintervals of 0.1 s each.

We see from Figure 8 that for the source field scale-length $L = 20$ km, the net transient field δE_x at $x = 0$ and $z = 30$ km has a highest peak that is about 50% of the source field strength E. For source fields with larger values of L, the peak value of $\delta E_x/E$ becomes smaller. Specifically, at $L > 100$ km the peak of $\delta E_x/E$ is less than 10%.

For the change in conductivity profile indicated by the dashed curves of Figure 4, we find that the net transient field $\delta E_x/E$ at $x = 0$ and $z = 30$ km has general properties similar to those in Figure 8; the peak value of $\delta E_x/E$ is high for small values of L and lower for larger values of L. For the same value of L, however, the peak value of $\delta E_x/E$ due to the conductivity change in Figure 4 is smaller than that of $\delta E_x/E$ due to the conductivity change in Figure 3. This is because the conductivity profile in Figure 3 allows the electric field to map down more efficiently than does the conductivity profile in Figure 4.

Distribution of Total Transient Electric Field E_x

In Figure 9 we show normalized total transient electric field E_x/E at $z = 30$ km and source scale-length $L = 20$ km as a function of normalized distance x/L for several time instants. The curves in this figure are drawn from the data obtained under the same condition as those for the curves in Figure 8. The curves of E_x/E (z= 30 km) for $t = 0$ and $t = \infty$ in Figure 9 are the solid curve and the dot-dash curve, respectively, for L = 20 km in Figure 6. A similar curve for any other value of t is the sum of the curve for $t = \infty$ and that of the corresponding net transient electric field $\delta E_x/E$, whose time variation is shown in Figure 8.

From Figure 9 we can see that as E_x increases, its x distribution approaches that of the source electric field at 150 km altitude, and as E_x decreases, its x-distribution approaches that at $t = \infty$. The reason for this is that field components of larger wave number k_x are more sensitive to change in the conductivity profile than those with smaller k_x. When E_x becomes stronger, its larger-k_x components increase more rapidly than its smaller-k_x components, thus making the x distribution of E_x more abrupt at the edge of the source field. Similarly, when E_x becomes weaker, its larger-k_x components decrease more rapidly than its smaller-k_x components, resulting in a smeared-out x distribution of E_x.

Time Variation of Net Transient Electric Field δE_z

Figure 10 shows the time variation of the normalized net transient electric field $-\delta E_z/\Delta\Phi$ at $x = L/2$ and $z = 0$ for $L = 20, 50$, and 100 km. The curves are drawn from data in the same problem as that for $\delta E_x/E$ ($x = 0, z = 30$ km) in Figure 8 and by a similar procedure. Comparing $-\delta E_z/\Delta\Phi$ with the steady state dc electric field $-E_z/\Delta\Phi$ ($x = L/2$, $z = 0$) in Figure 7*b*, we find that the peak values of δE_z for $L = 20$, 50, and 100 km are about 140%, 42%, and 42%, respectively, of the corresponding dc values. This agrees with the percentages of the peaks of δE_x (x = 0, z = 30 km) for different values of L, in comparison with the dc values of E_x ($x = 0, z = 30$ km) in Figure 6.

From the time variation of the electric fields in Figures 8 and 10 we find that the amplitude of δE_z at $z = 0$ decreases more slowly than does that of δE_x at $z = 30$ km. This is because the conductivity σ of the atmosphere at the ground level is lower than that at 30-km altitude, so that the attenuation rate of the electric field δE_z at $z = 0$ is lower than that of the electric field δE_x at $z = 30$ km.

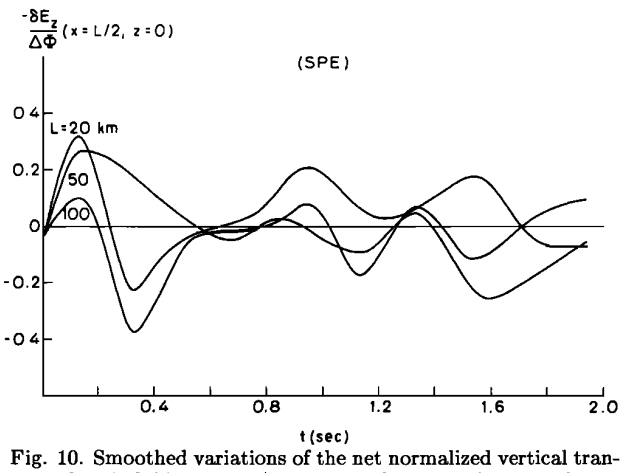

Fig. 10. Smoothed variations of the net normalized vertical transient electric field at $x = L/2$ and $z = 0$ following the same change in the conductivity profile as for the horizontal field in Figure 8.

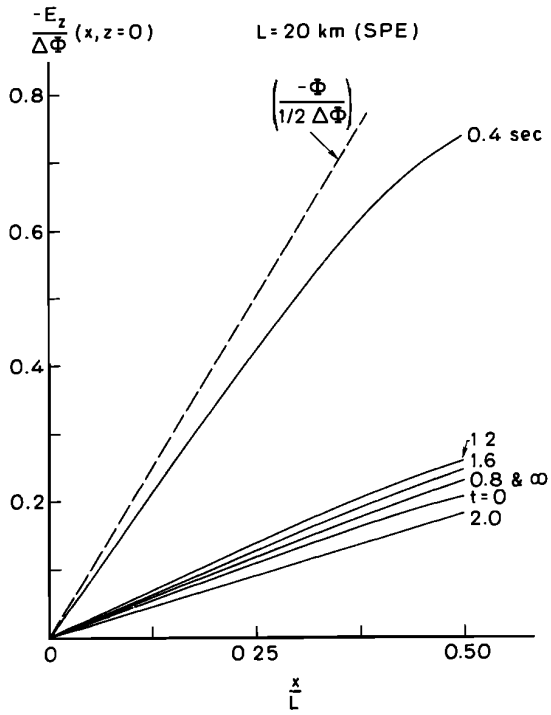

Fig. 11. Normalized vertical transient electric field on the ground plotted against normalized horizontal distance at several time instants. The dashed line shows the distribution of the normalized source potential at 150-km altitude.

Distribution of Total Transient Electric Field E_z

Figure 11 shows the x distribution of the total transient electric field $-E_z/\Delta\Phi$ at $z = 0$ and $L = 20$ km. The data for the curves in Figure 11 are obtained from the same problem as that for Figure 10. The curves are sums of the x variation of $-\delta E_z/\Delta\Phi$ and that of the dc field $-E_z/\Delta\Phi$ at $t = \infty$ from the dot-dash curve in Figure 7*b*.

In Figure 11 we observe that as the magnitude of E_z increases, the x distribution of $-E_z/\Delta\Phi$ approaches the dashed line $-\Phi/(\frac{1}{2}\Delta\Phi)$, which is the x distribution of the normalized source potential. This property of the total transient field E_z is similar to that of the total transient field E_x in Figure 9.

5. DISCUSSION AND CONCLUSIONS

The sudden changes in the conductivity profile of the atmosphere as indicated in Figures 3 and 4 result in tropospheric electric fields that vary with time before reaching a final dc steady state, which is different from the initial dc steady state before the change. For a source field scale-length $L = 20$ km, the dc electric field E_x ($z = 30$ km) in the final steady state as shown in Figure 5 is about 10% stronger than that in the initial steady state. For $L \geq 100$ km, E_x ($z = 30$ km) in the final steady state is less than 3% stronger than that in the initial steady state. Similarly, the dc electric field E_z ($z = 0$) at $L = 20$ km increases by ~20%, but that at $L \geq 100$ km increases by less than 4%. Since the solar-wind-induced source electric field in the ionosphere has a scale-length $L \simeq 3400$ km, then the steady state dc electric fields E_x and E_z in the troposphere will have a very small increase, which may not be observable, after the atmospheric profile has changed. During the change in conductivity profile, however, the horizontal distribution of the conductivity may not be uniform. This may then create horizontal electric fields with shorter scale-lengths in the ionosphere which map down to the troposphere [*Park*, 1976]. In this case the dc electric fields in the troposphere may undergo a sizeable change which can be observed in practice.

The effect of changes in the conductivity profile of the atmosphere on observed transient electric fields is similar to that on observed dc electric fields: a small-scale source field in the ionosphere produces observed transient fields of relatively high intensity compared to those produced by a large-scale source field at the same altitude. But, unlike dc electric fields, which change only slightly after a sudden change in conductivity profile, transient electric fields can have peaks that are comparable to or even exceed their steady state dc values. This is evident from Figures 8 and 10. It also suggests that effects of solar particle events and sudden energetic electron precipitation can be more easily detected by observing transient electric fields than by observing steady state dc electric fields.

For the transient electric field δE_x at 30-km altitude, its duration under the SPE effect as seen from Figure 8 is about 1.6 s. For the transient electric field δE_z at ground level, where the conductivity of the atmosphere is more than three orders of magnitude smaller than that at 30-km altitude, the duration is several minutes. Therefore, under the same change in conductivity profile of the atmosphere, δE_z at $z = 0$ will last longer than δE_x at $z = 30$ km and is more likely to be detected.

The results presented in this paper indicate that a sudden increase in the conductivity of the earth's atmosphere may result in significant transient electric fields in the troposphere when the horizontal source electric field in the ionosphere has a scale-length of order ~100-km or less. As noted above, field structures of this size are observed under various conditions near to and poleward of the plasmapause. In cases when a solar-wind-induced electric field of scale-length ~3000-km is the sole source, sudden changes in the conductivity profile would probably not be detectable through electric field measurements in the troposphere.

In terms of its applicability for detecting particle precipitation through associated ac electric fields, our results are most applicable to cases in which the scale size of precipitation regions are comparable to the scale size of the convection associated horizontal electric fields in the ionosphere. The size of burst precipitation regions is not well known; there are indications from pulsating aurora observations that some such regions are of order 50-100 km in extent [e.g. *Johnstone*, 1978]. However, when precipitation is nearly simultaneous on a number of magnetospheric paths excited by a single whistler source, the affected region may be of order 500 km or greater in extent [*Carpenter et al.*, 1985].

Further development of the model is needed. However, it provides a scientific motivation for conducting both long duration balloon measurements of the horizontal and vertical field and multipoint ground measurements of the vertical field. Such work might well be concentrated in the southern polar regions, where long duration circumpolar balloon flights are becoming increasingly practical and where a wide

range of magnetic latitudes are accessible for ground measurements in regions relatively free of thunderstorm activity.

APPENDIX

Equations for time-varying electromagnetic fields in an anisotropic layer of the earth's atmosphere at any time t are

$$\nabla \times \mathbf{E} = -(\mu_0)\frac{\partial \mathbf{H}}{\partial t} \qquad \nabla \times \mathbf{H} = \mathbf{J} + (\epsilon_0)\frac{\partial \mathbf{E}}{\partial t} \qquad \mathbf{J} = \vec{\sigma}(t)\mathbf{E} \tag{A1}$$

The term $\vec{\sigma}(t)$ represents the conductivity tensor as a function of time and, in this paper, can be expressed as

$$\vec{\sigma}(t) = \vec{\sigma}^- + (\Delta\vec{\sigma})u(t) \tag{A2}$$

where

$$\vec{\sigma}^- = \begin{pmatrix} \sigma_P^- & \sigma_H^- & 0 \\ -\sigma_H^- & \sigma_P^- & 0 \\ 0 & 0 & \sigma_0^- \end{pmatrix} \tag{A3}$$

$$\Delta\vec{\sigma} = \begin{pmatrix} (\sigma_P - \sigma_P^-) & (\sigma_H - \sigma_H^-) & 0 \\ -(\sigma_H - \sigma_H^-) & (\sigma_P - \sigma_P^-) & 0 \\ 0 & 0 & (\sigma_0 - \sigma_0^-) \end{pmatrix} \tag{A4}$$

$u(t)$ is the unit step function, $\sigma_0^-, \sigma_P^-, \sigma_H^-$ are the specific conductivity, Pedersen conductivity, and Hall conductivity, respectively, at $t < 0$ and $\sigma_0, \sigma_P, \sigma_H$ are the corresponding conductivities at $t > 0$.

We now eliminate $\mathbf{H}$ in equation (A1) by taking the curl of $\nabla \times \mathbf{E}$ and substituting for $\nabla \times \mathbf{H}$. This results in

$$\begin{aligned} \nabla\times(\nabla \times \mathbf{E}) &= -(\mu_0)\frac{\partial}{\partial t}\{\vec{\sigma}(t)\mathbf{E} + (\epsilon_0)\frac{\partial \mathbf{E}}{\partial t}\} \\ &= -(\mu_0)\{\vec{\sigma}(t)\frac{\partial \mathbf{E}}{\partial t} + (\epsilon_0)\frac{\partial^2 \mathbf{E}}{\partial t^2}\} - \mu_0(\Delta\vec{\sigma})\delta(t)\mathbf{E} \end{aligned} \tag{A5}$$

where the delta function $\delta(t)$ is the time derivative of $u(t)$. The quantity $\Delta\vec{\sigma}\delta(t)\mathbf{E}$ in the last term of equation (A5) represents conduction current density impulses at $t = 0$.

We will find $\mathbf{E}$ for $t > 0$ by using two approaches and show that, with continuity of the fields at t = 0, i.e.,

$$\mathbf{E}(0^+) = \mathbf{E}(0^-) \qquad \mathbf{H}(0^+) = \mathbf{H}(0^-) \tag{A6}$$

and with the initial fields in steady state, i.e.,

$$\mathbf{E}'(0^-) = \mathbf{0} \qquad \mathbf{H}'(0^-) = \mathbf{0} \tag{A7}$$

the two approaches lead to the same results.

In the first approach, we start observing the fields at t = 0^- and therefore retain the term containing $\delta(t)$ in equation (A5). Taking Laplace transforms on this equation with respect to time, noting from equations (A2)–(A4) that

$$\vec{\sigma}(t) = \vec{\sigma} = \begin{pmatrix} \sigma_P & \sigma_H & 0 \\ -\sigma_H & \sigma_P & 0 \\ 0 & 0 & \sigma_0 \end{pmatrix} \text{ for } \quad t > 0 \tag{A8}$$

we obtain

$$\begin{aligned} \nabla \times (\nabla \times \mathbf{E}_s) = &-\mu_0 s(\vec{\sigma} + \epsilon_0 s)\mathbf{E}_s + \mu_0\{(\vec{\sigma} + \epsilon_0 s)\mathbf{E}(0^-) \\ &+ \epsilon_0\mathbf{E}'(0^-)\} - \mu_0(\Delta\vec{\sigma})\mathbf{E}(0^-) \end{aligned} \tag{A9}$$

where $\mathbf{E}_s$ is the Laplace transformed function of $\mathbf{E}$.

Substituting from equations (A6) and (A7) into equation (A9) yields

$$\begin{aligned} \nabla \times (\nabla \times \mathbf{E}_s) = &-\mu_0 s(\vec{\sigma} + \epsilon_0 s)\mathbf{E}_s + \mu_0(\vec{\sigma} + \epsilon_0 s)\mathbf{E}(0^+) \\ &- \mu_0(\Delta\vec{\sigma})\mathbf{E}(0^+) \end{aligned} \tag{A10}$$

In the second approach, we start observing the fields at $t = 0^+$ so that we can set $\delta(t) = 0$ in Eq.(A-5), which then reduces to

$$\nabla \times (\nabla \times \mathbf{E}) = -\mu_0\{(\vec{\sigma})\frac{\partial \mathbf{E}}{\partial t} + (\epsilon_0)\frac{\partial^2 \mathbf{E}}{\partial t^2}\}, (t > 0) \tag{A11}$$

Equation (A11) can also be derived from the following set of equations:

$$\nabla \times \mathbf{E} = -(\mu_0)\frac{\partial \mathbf{H}}{\partial t} \qquad \nabla \times \mathbf{H} = \mathbf{J} + (\epsilon_0)\frac{\partial \mathbf{E}}{\partial t} \qquad \mathbf{J} = (\vec{\sigma})\mathbf{E} \tag{A12}$$

which is obtained from equation (A1) by simply replacing $\vec{\sigma}(t)$ for $t > 0$ with $\vec{\sigma}$ in equation (A8).

Taking Laplace transforms on equation (A11) with respect to time and using $t = 0^+$ as the starting point, we obtain

$$\begin{aligned} \nabla \times (\nabla \times \mathbf{E}_s) = &-\mu_0 s(\vec{\sigma} + \epsilon_0 s)\mathbf{E}_s + \mu_0(\vec{\sigma} + \epsilon_0 s)\mathbf{E}(0^+) \\ &+ \mu_0\epsilon_0\mathbf{E}'(0^+) \end{aligned} \tag{A13}$$

By taking the curl of equation (A6), we have $\nabla\times\mathbf{H}(0^+) = \nabla \times \mathbf{H}(0^-)$ which, by equations (A1) and (A7), leads to

$$\begin{aligned} \mathbf{J}(0^+) + \epsilon_0\mathbf{E}'(0^+) &= \mathbf{J}(0^-) + \epsilon_0\mathbf{E}'(0^-) \\ (\vec{\sigma})\mathbf{E}(0^+) + \epsilon_0\mathbf{E}'(0^+) &= (\vec{\sigma}^-)\mathbf{E}(0^-) = (\vec{\sigma}^-)\mathbf{E}(0^+) \end{aligned}$$

or

$$\epsilon_0\mathbf{E}'(0^+) = -(\vec{\sigma} - \vec{\sigma}^-)\mathbf{E}(0^+) = -(\Delta\vec{\sigma})\mathbf{E}(0^+) \tag{A14}$$

where equations (A3), (A4), and (A8) have been used.

Equation (A14) indicates that equation (A10) from the first approach is in fact equivalent to equation (A13) from the second approach. In conclusion, the current density impulses that occur at $t = 0$ due to the step change of the conductivity elements of $\vec{\sigma}(t)$ can be taken care of by the initial field conditions at $t = 0$ given in equations (A6) and (A7).

Acknowledgments. We are grateful to R. A. Helliwell for his continued support and encouragement throughout this research. We are grateful to the referees for helpful comments, in response to one of which the appendix is presented. The manuscript was prepared by N. Leger and G. Walker. This work was supported by the National Aeronautics and Space Administration under grant NGL-05-020-008, by the National Science Foundation, under grant ATM80-18248 and by the Fleischman Foundation. Computer facilities were sponsored in part by the National Center for Atmospheric Research in Boulder, Colorado.

REFERENCES

Arnoldy, R. L., K. Dragoon, L. J. Cahill, Jr., S. B. Mende, and T. J. Rosenberg, Detailed correlations of magnetic field obser-

vations at $L = 4.2$ with pulsating aurora, *J. Geophys. Res., 87*, 10,449, 1982.

Atkinson, W., S. Lundquist, and U. Fahleson, The electric field existing at stratospheric elevations as determined by tropospheric boundary conditions, *Pure Appl. Geophys., 39*, 1433, 1971.

Bostrom, R., and U. Fahleson, Vertical propagation of time-dependent electric fields in the atmosphere and ionosphere, paper presented at Fifty-First International Conference on Atmospheric Electricity, Garmisch-Partenkirchen, Federal Republic of Germany, Sept. 2–7, 1974.

Bostrom, R., U. Fahleson, L. Olaasson, and G. Hallendal, Theory of time-varying atmospheric electric fields and some applications to fields of ionospheric origin, *Tech. Rep. TRITA-EPP-73-02*, R. Inst. of Technol., Stockholm, Sweden, 1973.

Carpenter, D. L., U. S. Inan, E. W. Paschal, and A. J. Smith, A new VLF method for studying burst precipitation near the plasmapause, *J. Geophys. Res., 90*, 4383, 1985.

Chang, H.-C., and U. S. Inan, Lightning-induced electron precipitation from the magnetosphere, *J. Geophys. Res., 90*, 1531, 1985.

Chiu, Y. T., Self-consistent electrostatic field mapping in the high-latitude ionosphere, *J. Geophys. Res., 79*, 2790, 1974.

de la Beaujardiere, O., R. Vondrak, R. Heelis, W. Hanson, and R. Hoffman, Auroral arc electrodynamic parameters measured by AE-C and the Chatanika radar, *J. Geophys. Res., 86*, 4671, 1981.

Dejnakarintra, M., A theoretical study of electrical coupling between the troposphere, ionosphere, and magnetosphere, *Tech. Rep. 3454-3*, Radio Sci. Lab., Stanford Univ., Stanford, Calif., 1974.

Dejnakarintra, M. A theoretical study of transient electric fields in the troposphere following a step change in the atmospheric conductivity profile, *Tech. Rep. E4-2322*, Space, Telecomm. and Radiosci. Lab., Stanford Univ., Stanford, Calif., 1983.

Dejnakarintra, M., and C. G. Park, Lightning-induced electric fields in the ionosphere, *J. Geophys. Res., 79*, 1903, 1974.

Doolittle, J. H., Modification of the ionosphere by VLF wave-induced electron precipitation, *Tech. Rep. E4-21301318*, Radio Sci. Lab., Stanford Univ., Stanford, Calif., 1982.

Engebretson, M. J., L. J. Cahill, R. L. Arnoldy and T. J. Rosenberg, Correlated magnetic pulsation emissions at Siple Station, Antarctica, *J. Geophys. Res., 88*, 4841, 1983.

Farley, D. T., Jr., A theory of electrostatic fields in a horizontally stratified ionosphere subject to vertical magnetic field, *J. Geophys. Res., 64*, 1225, 1959.

Heppner, J. P., Electric field variations during substorms - OGO 6 measurements, *Planet. Space Sci., 20*, 1475, 1972.

Inan, U. S., T. F. Bell, and H. C. Chang, Particle precipitation induced by short-duration VLF waves in the magnetosphere, *J. Geophys. Res., 87*, 6243, 1982.

Johnstone, A. D., Pulsating aurora, *Nature, 274*, 119, 1978.

Maynard, N. C., J. P. Heppner and A. Egeland, Intense variable electric fields at ionospheric altitudes in the high latitude regions as observed by DE 2, *Geophys. Res. Lett., 9*, 981, 1982.

Mozer, F. S., Electric field mapping in the ionosphere at the equatorial plane, *Planet. Space Sci., 18*, 259, 1970.

Park, C. G., Downward mapping of high-latitude ionospheric electric fields to the ground, *J. Geophys. Res., 81*, 168, 1976.

Park, C. G., Comparison of two-dimensional and three-dimension al mapping of ionospheric electric fields, *J. Geophys. Res., 84*, 960, 1979.

Park, C. G., and M. Dejnakarintra, Penetration of thundercloud electric fields into the ionosphere and magnetosphere, l., Middle and subauroral altitudes, *J. Geophys. Res., 78*, 6623, 1973.

Park, C. G., and M. Dejnakarintra, The effects of magnetospheric convection on atmospheric electric fields in the polar cap, paper presented at Fifty-First International Conference on Atmospheric Electricity, Garmisch-Partenkirchen, Federal Republic of Germany, Sept. 2–7, 1974.

Park, G. K. Microburst precipitation phenomena, *J. Geomagn. Geoelectr., 30*, 327, 1978.

Reagan, J. B., R. E. Meyerott, J. E. Evans, and W. L. Imhof, The effects of energetic-particle precipitation on the global atmospheric electric circuit, paper presented at Sixth International Atmospheric Electricity Conference, Manchester, England, July 1980.

Reid, G. C., Ionospheric effects of electrostatic fields generated in the outer magnetosphere, *Radio Sci., 69D*, 827, 1965.

Rishbeth, H., and O. K. Garriott, *Introduction to Ionospheric Physics*, p. 137, Academic, Orlando, Fla., 1969.

Rosenberg, T. J., J. C. Siren, D. L. Matthews, K. Marthinsen, J. A. Holtet, A. Egeland, D. L. Carpenter, and R. A. Helliwell, Conjugacy of electron microbursts and VLF chorus, *J. Geophys. Res., 86*, 5819, 1981.

Smiddy, M., M. C. Kelley, W. Burke, F. Rich, R. Sagalyn, B. Shuman, R. Hays, and S. Lai, Intense poleward-directed electric fields near the ionospheric projection of the plasmapause, *Geophys. Res. Lett., 4*, 543, 1977.

Spreiter, J. R., and B. Briggs, Theory of electrostatic fields in the ionosphere at polar and middle geomagnetic latitudes, *J. Geophys. Res., 66*, 1731, 1961.

Volland, H., Global quasi-static electric fields in the earth's environment, paper presented at Fifty-First International Conference on Atmospheric Electricity, Garmisch-Partenkirchen, Federal Republic of Germany, Sept. 2–7, 1974.

D. L. Carpenter and U. S. Inan, STAR Laboratory, Stanford University, Stanford, CA 94305.

M. Dejnakarintra, Department of Electrical Engineering, Chulalongkorn University, Bangkok 10505, Thailand.

(Received January 18, 1985;
revised July 22, 1985;
accepted July 23, 1985.)